NJC

ROYAL SOCIETY OF CHEMISTRY

PAPER

View Article Online
View Journal | View Issue

Cite this: *New J. Chem.*, 2025, **49**, 15691

Magnetic superexchange couplings in doubly bis(2-pyridyl)pyrazolato-bridged dinuclear copper(II) complexes

Miku Kawano,[a] Ying-Ying Wu,[b] Zhao-Yang Li,[b] Akio Mishima,[a] Satoshi Kawata[a] and Ryuta Ishikawa*[a]

Received 12th May 2025,
Accepted 16th August 2025

DOI: 10.1039/d5nj02006a

rsc.li/njc

The solvothermal reaction of $CuCl_2{\cdot}2H_2O$ with 3,5-bis(2-pyridyl)pyrazole (Hbpypz) in a methanol/water mixed solvent produces a dinuclear Cu^{II} complex, formulated as *syn*-$[Cu_2(\mu\text{-bpypz})_2Cl_{1.5}(H_2O)_{0.5}]Cl_{0.5}{\cdot}3H_2O$. Single-crystal X-ray diffraction analysis revealed that the two Cu^{II} centres were in a distorted square-pyramidal coordination environment. The basal plane of each Cu^{II} centre was bridged by two unique bis-bidentate $bpypz^-$ ligands. One of the apical coordination sites showed disorder and was occupied by chloride or water. In contrast, the other apical site was solely occupied by chloride with no disorder. The apical coordination sites of the two Cu^{II} centres adopted a *syn*-configuration across the $Cu_2(\mu\text{-bpypz})_2$ basal plane. Variable-temperature static magnetic susceptibility measurements indicated a strong antiferromagnetic interaction of $-191.52\ cm^{-1}$ between the Cu^{II} centres, mediated by the doubly $bpypz^-$ bridging ligands. Broken-symmetry DFT calculations were performed using various characteristic functionals with different basis sets to investigate magnetic superexchange couplings in detail. The global hybrid GGA PBE0 functional, combined with the def2-TZVP basis set and ZORA relativistic approximation, provided the most accurate results, closely reproducing the experimental magnetic exchange values. These computational approaches were validated by their successful application to related complexes.

Introduction

Magnetic superexchange coupling (J) plays a pivotal role in determining the magnetic properties of multinuclear metal complexes. The superexchange mechanism for magnetic coupling in molecular systems operates when sufficient orbital overlap exists between the paramagnetic metal orbitals and bridging ligand orbitals.[1–4] In multinuclear metal complexes, the energy separation between the spin ground state and excited states is directly related to the magnitude and sign of J. This parameter is typically determined using variable-temperature static magnetic susceptibility data analysed using the isotropic Heisenberg–Dirac–van Vleck (HDvV) spin Hamiltonian.[5,6] A comprehensive understanding of magnetic interactions encompassing both experimental observations and theoretical insights is essential for designing molecule-based magnetic materials and advancing fundamental research in magnetism.

Among various bridging ligands, 3,5-bis(2-pyridyl)pyrazole (Hbpypz) has gained attention owing to its ability to form stable multinuclear complexes.[7–10] Upon deprotonation, Hbpypz transforms into its monoanionic form, $bpypz^-$, which acts as a bidentate ligand. Depending on the coordination environment, one,[11–35] two,[36–56] or three[57–69] $bpypz^-$ ligands can coordinate to the metal centres, enabling the formation of diverse multinuclear metal complexes. Typically, $bpypz^-$ ligands generate homodinuclear metal complexes under mild conditions by simply mixing a metal salt solution with a Hbpypz solution at ambient temperature, where *in situ* deprotonation occurs without requiring additional bases. Structurally, these homodinuclear complexes feature two metal centres bridged by two pyrazolate units, with 3,5-disubstituted 2-pyridyl arms coordinating equatorially.[36–56]

A particularly well-studied subset of these complexes comprises five-coordinate homomultinuclear Cu^{II} complexes bearing various apical co-ligands, all incorporating a $Cu_2(\mu\text{-bpypz})_2$ core. Within this framework, antiferromagnetic exchange coupling arises between the unpaired electrons at each Cu^{II} centre, mediated by the two pyrazolate bridges of the doubly $bpypz^-$-bridged structure.[37,38,44,50,54,55]

Recent advances have deepened our understanding of the magnetostructural correlations in these dinuclear Cu^{II} complexes.[70,71] Building upon these findings, we aimed to explore their magnetic properties in greater detail.

Herein, we report the synthesis, X-ray structural characterisation, and magnetic properties of a novel doubly $bpypz^-$-bridged

[a] *Department of Chemistry, Faculty of Science, Fukuoka University, 8-19-1 Nanakuma, Jonan-ku, Fukuoka 814-0180, Japan. E-mail: ryutaishikawa@fukuoka-u.ac.jp*
[b] *School of Materials Science and Engineering, Nankai University, Tianjin 300350, P. R. China*

dinuclear Cu^{II} complex. Additionally, we used theoretical calculations involving the broken-symmetry (BS) approach[72–78] based on the unrestricted Kohn–Sham density functional theory (UKS-DFT) to gain deeper insight into the magnetic superexchange couplings in this complex and the related $Cu_2(\mu\text{-bpypz})_2$ frameworks.

Results and discussion

Synthesis and identification

Green block-shaped crystals were obtained from the solvothermal reaction of $CuCl_2{\cdot}2H_2O$ in water with an equimolar amount of Hbpypz in methanol under autogenous pressure at 160 °C for three days (Scheme 1). The resulting crystals were characterised by single-crystal X-ray diffraction (SCXRD) (Table S1), thermogravimetric analysis (TGA) (Fig. S1), and elemental analysis (EA), and were identified as *syn*-$[Cu_2(\mu\text{-bpypz})_2Cl_{1.5}(H_2O)_{0.5}]Cl_{0.5}{\cdot}3H_2O$ (**1**). The phase purity was also confirmed using powder X-ray diffraction (PXRD) measurements (Fig. S2).

Single-crystal X-ray structure

Complex **1** crystallises in the triclinic space group $P\bar{1}$ (Table S1). The asymmetric unit consisted of a Cu^{II} dimeric unit, a half-uncoordinated chloride ion, and three interstitial water molecules, which were disordered and modelled over four unequal occupancies in the crystal lattice. The number of water molecules was consistent with the TGA data, and the chemical formulation determined from EA matched the data obtained (Experimental details in SI).

The dinuclear unit comprises two unique Cu^{II} centres, where two $bpypz^-$ ligands chelate and bridge the Cu^{II} centres in a (N', $N1$, $N2$, N'')$_2$ double-bridging coordination mode. One Cu^{II} centre binds four nitrogen atoms from two independent $bpypz^-$ ligands in the equatorial site and a chloride ion in the apical site, forming a distorted square pyramidal coordination environment with a geometry index (τ) of 0.12(7), defined as $\tau = |\theta - \varphi|/60°$, where θ and φ are the two largest angles in the coordination sphere.[79] Remarkably, the other Cu^{II} centre also adopts a distorted square pyramidal coordination environment with τ = 0.11(7), but the chloride ion and oxygen atom of the water molecule are disordered at the apical coordination site, each with an occupancy of 0.5 (Fig. 1). Consequently, half the chloride ions and water molecules were coordination-free in the crystal lattice.

The average equatorial Cu–N(pyrazolate) and Cu–N(pyridyl) distances are 1.949(2) and 2.085(2) Å, respectively, while the average apical Cu–Cl and Cu–O distances of 2.504(3) and 2.242(8) Å are significantly longer than those of the equatorial bonds owing to the Jahn–Teller distortion.[80,81] The intramolecular Cu···Cu distance *via* the doubly $bpypz^-$-bridges is 4.0188(4) Å. These bond distances were similar to those observed in complexes with doubly $bpypz^-$-bridged Cu^{II} dinuclear frameworks.[37,38,44,48,50,51,54,55]

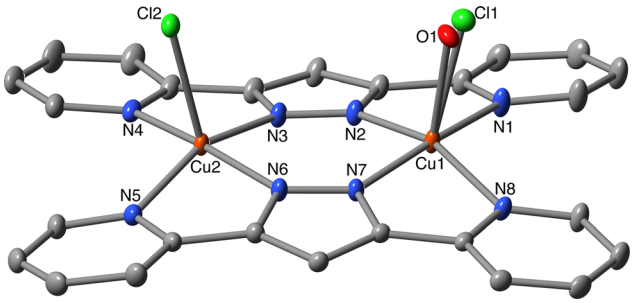

Fig. 1 Crystal structure of **1** with thermal ellipsoids drawn at a 50% probability level. The orange, light-green, blue, red, and gray ellipsoids represent Cu, Cl, N, O, and C atoms, respectively. Cl^- counterion, lattice H_2O molecules and H atoms are omitted for clarity.

The dimeric units of **1** are connected *via* π–π stacking interactions between the pyrazolate and pyridyl rings within the $bpypz^-$ ligands, forming π–π stacked tetramers, with the closest intermolecular Cu···Cu separation of 4.5091(3) Å. These tetramers are further linked through π–π stacking and hydrogen-bonding interactions in the crystal packing.

Magnetic property

The direct-current (DC) molar magnetic susceptibility (χ_M) measurement was performed on crushed crystalline samples of **1** in the temperature range of 2–300 K, with an applied magnetic field of 0.1 T (Fig. 2 and Fig. S3). As the temperature decreased, the χ_M values decreased to a minimum of approximately 0.00015 $cm^3\ mol^{-1}$ at 70 K and then remained nearly constant down to 20 K, indicating the presence of temperature-independent paramagnetism (TIP). Below this temperature, the χ_M values increased rapidly with decreasing temperature, reflecting a small amount of Cu^{II} monomeric impurities. To assess the strength of the antiferromagnetic coupling constant, J, the χ_M *versus* temperature data was analysed using the Bleaney–Bowers equation (eqn (1)),[82] derived from the isotropic HDvV spin Hamiltonian, $\hat{H}_{HDvV} = -2J\hat{S}_A{\cdot}\hat{S}_B$ ($S_A = S_B = 1/2$):[5,6]

$$\chi_M = (1-f)\frac{2N_A g^2 \mu_B{}^2}{k_B T}\left[3+\exp\left(-\frac{\Delta E}{k_B T}\right)\right]^{-1} + f\frac{N_A g^2 \mu_B{}^2}{3k_B T}S(S+1) + \mathrm{TIP} \quad (1)$$

where N_A is the Avogadro constant, g is the isotropic Landé g factor, μ_B is the Bohr magneton, k_B is the Boltzmann constant,

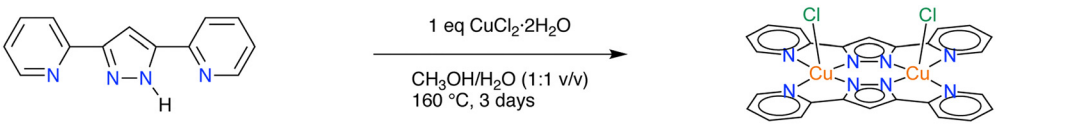

Scheme 1 Synthesis method of the complex **1**.

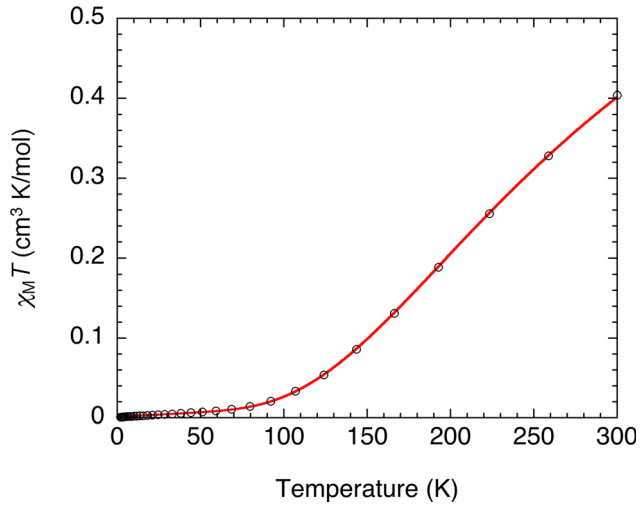

Fig. 2 Plots of the molar magnetic susceptibility times temperature ($\chi_M T$) *versus* temperature for **1** under an applied field of 0.1 T. The solid red curve indicates fit to the data using eqn (1).

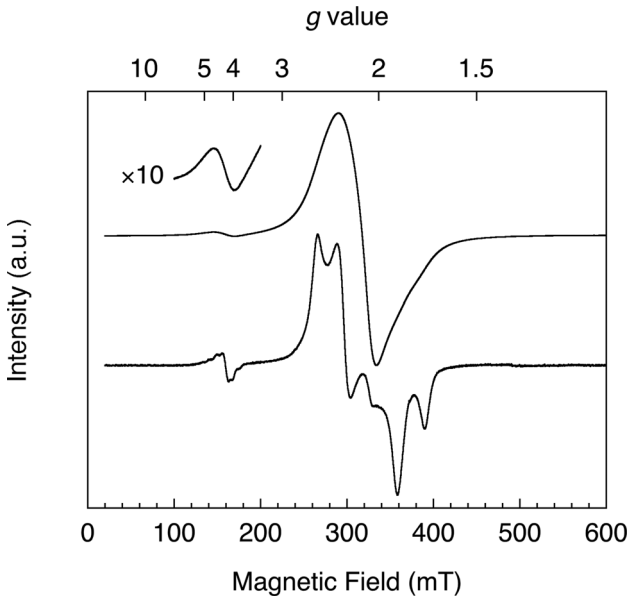

Fig. 3 CW X-band ESR spectra of crushed crystalline samples of **1** collected at 300 (upper) and 100 K (lower), highlighting the ΔM_S = 2 transitions at 300 K.

T is the absolute temperature, ΔE (= $-2J$) is the energy gap between the excited triplet (S = 1) and ground singlet states (S = 0), and S_A and S_B represent the spin quantum numbers for each Cu^{II} centre. Additionally, the fraction of Cu^{II} monomeric impurities (f) with g = 2 and S = 1/2 and TIP (60×10^{-6} cm^3 mol^{-1} per Cu^{II} site) are included in the equation.[2] This model provided a good fit to the DC magnetic data across the entire temperature range of 2 to 300 K, yielding g = 2.12(1), $J = -191.52(7)$ cm^{-1}, and f = 0.0025(2). The J value for complex **1** was comparable to those of previously reported complexes featuring the Cu$_2$(μ-bpypz)$_2$ framework.[37,44,50,54,55]

Continuous-wave X-band electron spin resonance spectroscopy

To further investigate the magnetic properties of **1**, continuous-wave (CW) X-band electron spin resonance (ESR) measurements were performed on the crushed crystalline samples over the temperature range of 100–300 K (Fig. 3 and Fig. S4). The CW X-band ESR spectra of **1** exhibit characteristic features of an excited triplet spin state of S = 1, displaying a strong full-field transition (allowed ΔM_S = 1 transition) at approximately $g \approx 2$ and a weak half-field transition (forbidden ΔM_S = 2 transition) at approximately g = 4.[1] The intensity of these transitions decreases significantly as the temperature decreases. Notably, as the temperature decreased from 300 to 100 K, the spectral resolution of the signals improved (Fig. S4). The CW X-band ESR spectra could be quantitatively analysed using the spin Hamiltonian given by eqn (2):

$$\hat{\mathcal{H}} = D\left[\hat{S}_z^2 - \frac{S(S+1)}{3}\right] + E\left(\hat{S}_x^2 - \hat{S}_y^2\right) + \boldsymbol{g}\mu_B\hat{\boldsymbol{S}}\boldsymbol{B} \qquad (2)$$

where D and E correspond to the axial and rhombic zero-field splitting parameters, $\hat{S}_x$, $\hat{S}_y$, and $\hat{S}_z$ are the spin operators for the excited triplet state (S = 1), $\boldsymbol{g}$ represents the Landé g factor (g_x, g_y, g_z), $\hat{\boldsymbol{S}}$ is the spin operator of the excited triplet state (S = 1), and $\boldsymbol{B}$ is the external magnetic field. The best-fit simulation parameters obtained from the CW X-band ESR spectra are $D = -0.05851(3)$ cm^{-1}, E/D = 0.0100, g_z = 2.2642(4), and $g_{x,y}$ = 2.0572(1) (Fig. S5).[83] These values are consistent with those reported for related multinuclear Cu(II) complexes featuring a Cu$_2$(μ-bpypz)$_2$ framework.[37,44,50,54,55]

Theoretical calculations

Multireference and multiconfigurational wavefunction methods are essential for accurately describing the magnetic superexchange coupling. The complete active space self-consistent field (CASSCF)[84] method is widely used because of its ability to capture static electron correlation. In contrast, dynamic electron correlation can be addressed using complete-active-space second-order perturbation theory (CASPT2)[85,86] or N-electron valence state second-order perturbation theory (NEVPT2).[87,88] Recent advances, including the density matrix renormalisation group (DMRG),[89–93] have further extended CASSCF to accommodate larger active spaces, enabling the study of exchange-coupled multinuclear metal complexes with many electrons. The difference-dedicated configuration interaction (DDCI)[94–96] and multireference coupled-cluster (MRCC)[97,98] methods are recognised as being the most accurate approaches for describing magnetic interactions. However, the high computational cost and expertise required for their application remain significant barriers to their routine use in paramagnetic transition metal complexes.

Alternatively, the BS UKS-DFT approach offers a practical and computationally efficient method for investigating magnetic superexchange coupling. BS UKS-DFT circumvents the need for multireference wavefunction calculations by using a single-determinant framework, significantly reducing computational demands, while still providing reasonable approximations of magnetic interactions. Spin projection schemes, such as the

Noodleman and Yamaguchi equations,[72–76] have been applied to mitigate spin contamination in low-spin states to improve the accuracy of BS UKS-DFT a robust and accessible alternative to wavefunction-based methods, facilitating routine exploration of magnetic properties of spin-coupled systems.

Therefore, quantum chemical calculations[99,100] were performed using the BS approach based on UKS-DFT to quantitatively describe the magnetic superexchange coupling constant (J) between the Cu^{II} centres *via* double $bpypz^-$ bridges in **1**.

The apical coordination site on one of the two Cu^{II} centres in **1** is disordered and occupied by either a chloride ion or the oxygen atom of a water molecule. Therefore, a model structure, *syn*-$[Cu_2(\mu\text{-bpypz})_2Cl_2]$ (**1′**), was used, in which all counterions and lattice solvents were removed, and only the positions of all hydrogen atoms were optimised using the B97-3c density functional with def2-mTZVP and def2-mTZVP/J basis sets (Fig. 4 and 5).[101] The model complex **1′** was used to evaluate the effects of different density functionals.

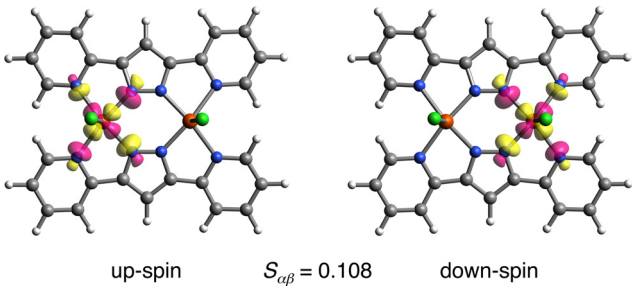

Fig. 4 BS UCOs (isovalue = 0.05) of **1′**, calculated using the PBE0 density functional with ZORA-def2-TZVP basis set for all atoms. Yellow and magenta surfaces indicate positive and negative spin phases.

The initial test evaluated the performance of five density functionals using the re-contracted zeroth-order regular approximation (ZORA) def2-TZVP basis set,[102] along with the corresponding segmented all-electron relativistically contracted auxiliary basis set (SARC/J)[103] for all atoms. Additionally, the ZORA scalar relativistic Hamiltonian[104] was incorporated.

The five density functionals tested included the generalised gradient approximation (GGA) BP86,[105,106] hybrid meta-GGA TPSSh,[107] global hybrid GGAs B3LYP[108,109] and PBE0,[110,111] and range-separated hybrid ωB97M-D3BJ[112] functionals. The theoretical magnetic superexchange coupling constants (J_{DFT}) estimated from BS-UKS DFT calculations are summarised in Table 1 and were calculated using the spin projection formalism (eqn (3)) proposed by Yamaguchi *et al.*:[75,76]

$$J_{DFT} = \frac{E_{BS} - E_{HS}}{\langle \hat{S}^2 \rangle_{HS} - \langle \hat{S}^2 \rangle_{BS}} \quad (3)$$

where E_{HS} and E_{BS} represent the energies of the ferromagnetic high-spin (HS) state (S = 1) and the antiferromagnetic BS state (S = 0), respectively, while $\langle \hat{S}^2 \rangle_{HS}$ and $\langle \hat{S}^2 \rangle_{BS}$ are the expectation values of the corresponding spin operators. In all cases, the HS state was found to have a higher energy than that of the BS state, confirming the presence of antiferromagnetic interactions between the Cu^{II} centres, as evidenced by the computed J_{DFT} values. Among the tested density functionals, the GGA BP86 functional severely overestimates the energy gap $E_{HS} - E_{BS}$, leading to an overly large J_{DFT} value. Conversely, the range-separated hybrid ωB97M-D3BJ functional underestimated $E_{HS} - E_{BS}$, resulting in a significantly smaller J_{DFT} value. The global hybrid GGA B3LYP and hybrid meta-GGA TPSSh functionals slightly overestimated $E_{HS} - E_{BS}$, yielding somewhat larger J_{DFT} values than expected. Among the five functionals tested, the global

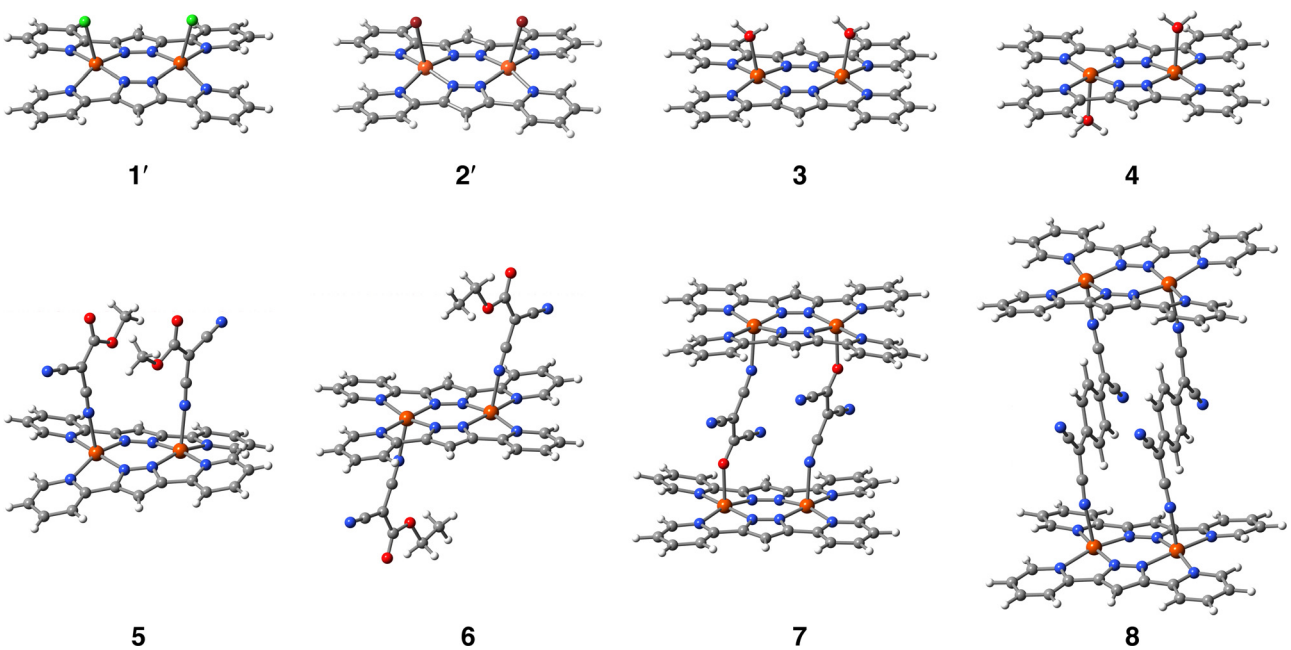

Fig. 5 Molecular structures for **1′–8** calculated in this work. The orange, light green, blue, red, gray, and white spheres represent Cu, Cl, N, O, C, and H atoms, respectively. Atomic coordinates were taken from the crystal structure and positions of only H atoms were optimized geometrically.

Table 1 Summary of E_{HS}, E_{BS}, $\langle \hat{S}^2 \rangle_{HS}$, $\langle \hat{S}^2 \rangle_{BS}$, and J_{DFT}, for **1′** obtained from BS UKS-DFT calculations at five different density functionals with the ZORA-def2-TZVP and SARC/J basis sets. The experimental J value is −191.52 cm^{-1}

Functional	E_{HS} (E_h)	E_{BS} (E_h)	$\langle \hat{S}^2 \rangle_{HS}$	$\langle \hat{S}^2 \rangle_{BS}$	J_{DFT} (cm^{-1})
BP86	−5692.883609	−5692.887430	2.0052	0.8119	−702.70
TPPSh	−5692.323681	−5692.325242	2.0062	0.9723	−331.21
B3LYP	−5691.089335	−5691.090453	2.0062	0.9886	−241.11
PBE0	−5689.721757	−5689.722635	2.0067	0.9956	−190.54
ωB97M-D3BJ	−5692.674508	−5692.675172	2.0055	1.0001	−145.05

hybrid GGA PBE0 functional agreed best with the experimentally determined J value (the absolute percentage error was only 1%). Therefore, the global hybrid GGA PBE0 function was the best for describing the magnetic properties of the $Cu_2(\mu\text{-bpypz})_2$ framework. The magnitude of J_{DFT} computed *via* the BS-UKS DFT method is acknowledged as being dependent on the fraction of Hartree–Fock (HF) exchange included in the functional.[113,114] Generally, the value of J_{DFT} decreases as the percentage of HF exchange increases. This trend was observed among the tested functionals, with TPSSh (10%), B3LYP (20%), and PBE0 (25%) exhibiting systematic reductions in $E_{HS} - E_{BS}$. The BP86 functional, which lacks HF exchange, exhibited a significantly larger $E_{HS} - E_{BS}$ than that of the hybrid functionals. However, the underestimation of $E_{HS} - E_{BS}$ by the ωB97M-D3BJ functional (which includes 15% short-range and 100% long-range HF exchange) may be attributed to the density overdelocalisation inherent in the range-separated scheme. Furthermore, using the PBE0 functional, the influence of ZORA on the total energy was examined, and it was small but not negligible (Table S2).

To investigate the influence of the basis sets on the computed magnetic superexchange coupling, five recontracted ZORA-def2-type basis functions of varying quality were tested using the global hybrid GGA PBE0 density functional. Table 2 summarises the computed J_{DFT} values and the related parameters for **1′**. Among the basis sets tested, the split-valence basis function (ZORA-def2-SVP) overestimated the energy gap of $E_{HS} - E_{BS}$, resulting in a relatively large negative J_{DFT} value. By contrast, the mono-polarised triple-ζ valence basis sets (ZORA-def2-TZVP(−f) and ZORA-def2-TZVP) provided well-balanced J_{DFT} values that closely matched the experimental data. Further, the doubly polarised triple-ζ and quadruple-ζ valence basis sets (ZORA-def2-TZVPP and ZORA-def2-QZVPP) led to a reduction in $E_{HS} - E_{BS}$, yielding less negative J_{DFT} values. These findings suggest that mono-polarised triple-ζ valence quality basis sets such as ZORA-def2-TZVP are optimal for accurately predicting J_{DFT} when using the global hybrid GGA PBE0 density functional. As predicted by canonical crystal field theory, the square

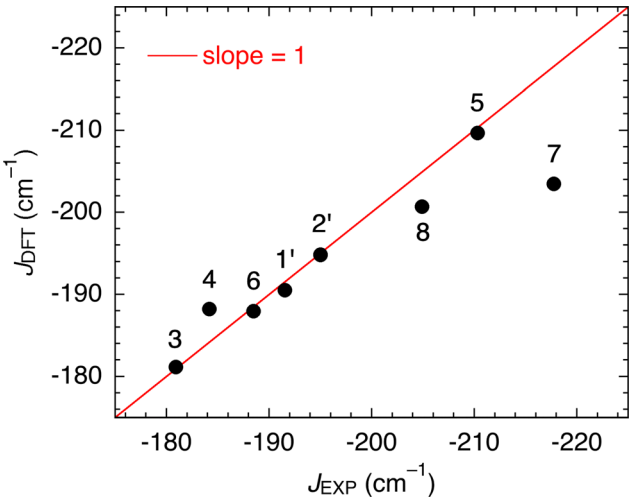

Fig. 6 Comparison of correlations between BS UKS-DFT computed (J_{DFT}) and experimental (J_{EXP}) exchange coupling constants.

pyramidal Cu^{II} centre exhibits the characteristic d-orbital splitting pattern: $d_{x^2-y^2} > d_{z^2} > d_{xy} > d_{xz} \approx d_{yz}$. In this configuration, the unpaired electron primarily occupies the highest-energy $d_{x^2-y^2}$ orbital due to the $3d^9$ electronic configuration. Consistent with this prediction, the unrestricted corresponding orbitals (UCOs) for model complex **1′** in the BS state predominantly involve the $d_{x^2-y^2}$ orbitals of both Cu^{II} centres, as well as the sp^2 hybrid orbitals of the coordinating nitrogen atoms in the doubly bridged $bpypz^-$ ligands, which contribute lone pair electrons. By contrast, the chloride ligand at the apical position contributed minimally to the UCOs (Fig. 4). The overlap integral ($S_{\alpha\beta}$) between the UCOs is significantly smaller than 1, suggesting a high degree of spin polarisation. Indeed, the spin density is delocalised across both Cu^{II} centres (0.662794 e and −0.663932 e, respectively) and the coordinating nitrogen atoms (0.104385 e, −0.103594 e, 0.094435 e, and −0.095416 e), indicating the presence of σ-type magnetic superexchange pathways. This σ-type orbital overlap between the $d_{x^2-y^2}$ magnetic orbitals facilitates strong magnetic superexchange coupling.

To further validate the performance of the PBE0/ZORA-def2-TZVP method, additional computations were performed on seven related complexes: *syn*-$[Cu_2(\mu\text{-bpypz})_2Br_{1.25}(H_2O)_{0.75}]Br_{0.75}\cdot 2.25H_2O$ (**2**),[50] *syn*-$[Cu_2(\mu\text{-bpypz})_2(H_2O)_2](NO_3)_2\cdot H_2O$ (**3**),[37] *anti*-$[Cu_2(\mu\text{-bpypz})_2(H_2O)_2](ClO_4)_2$ (**4**),[44] *syn*-$[Cu_2(\mu\text{-bpypz})_2(DCNM)_2]$ (**5**),[54] *anti*-$[Cu_2(\mu\text{-bpypz})_2(DCNE)_2]$ (**6**),[54] $[Cu_4(\mu\text{-bpypz})_4(\mu\text{-TCVA})_2]\cdot 2TCVA$ (**7**),[54] and $[Cu_4(\mu\text{-bpypz})_4(\mu\text{-TCNQ})_2]\cdot 2TCNQ$ (**8**)[55] (Fig. 4). The ligand abbreviations are as follows: $DCNM^-$ = 2,2-dicyano-1-methoxyethenolate, $DCNE^-$ = 2,2-dicyano-1-ethoxyethenolate,

Table 2 Summary of J_{DFT}, E_{HS}, E_{BS}, $\langle \hat{S}^2 \rangle_{HS}$ and $\langle \hat{S}^2 \rangle_{BS}$ for **1′** obtained from BS UKS-DFT calculations at the global hybrid GGA PBE0 density functional with five different quality of def2-type basis and SARC/J auxiliary basis sets. The experimental J value is −191.52 cm^{-1}

Basis function	E_{HS} (E_h)	E_{BS} (E_h)	$\langle \hat{S}^2 \rangle_{HS}$	$\langle \hat{S}^2 \rangle_{BS}$	J_{DFT} (cm^{-1})
ZORA-def2-SVP	−5687.245522	−5687.246542	2.0062	0.9939	−221.12
ZORA-def2-TZVP(−f)	−5689.682279	−5689.683165	2.0066	0.9955	−192.30
ZORA-def2-TZVP	−5689.721757	−5689.722635	2.0067	0.9956	−190.54
ZORA-def2-TZVPP	−5689.733296	−5689.734147	2.0067	0.9961	−184.74
ZORA-def2-QZVPP	−5689.954905	−5689.955741	2.0067	0.9963	−181.56

Table 3 Summary of E_{HS}, E_{BS}, $\langle \hat{S}^2 \rangle_{HS}$, $\langle \hat{S}^2 \rangle_{BS}$, J_{DFT}, and experimental J for **1′–8** obtained from BS UKS-DFT calculations at the global hybrid GGA PBE0 density functional with the ZORA-def2-TZVP and SARC/J basis sets

Complex	E_{HS} (E_h)	E_{BS} (E_h)	$\langle \hat{S}^2 \rangle_{HS}$	$\langle \hat{S}^2 \rangle_{BS}$	J_{DFT} (cm^{-1})	J^a (cm^{-1})	CSD ID[c]
1′	−5689.721757	−5689.722635	2.0067	0.9956	−190.54	−191.52	This work
2′	−10 013.281500	−10 013.282398	2.0065	0.9950	−194.82	−195.0	REGVIK
3	−4917.535023	−4917.535858	2.0063	0.9941	−181.18	−180.9	CAPXOK
4	−4917.542906	−4917.543774	2.0062	0.9936	−188.23	−184.15	FESQUQ
5	−5669.679006	−5669.679974	2.0063	0.9936	−209.67	−210.30	LIZFAE
6	−5784.312022	−5748.312889	2.0064	0.9946	−187.96	−188.47	LIZDUW
7	−11 250.031499	−11 250.033375	6.0126	1.9866	−203.22[b]	−217.74	LIZFIM
8	−12 244.280338	−12 244.280236	20.0753	4.0741	−200.81[b]	−204.90	LOZPEY

[a] Value were fitted using spin Hamiltonian, $\hat{H}_{HDvV} = -2J_{AB}\hat{S}_A \cdot \hat{S}_B$ ($S_A = S_B = 1/2$). [b] Values were obtained using the general algorithm for magnetic coupling constants in multispin systems (see SI).[115] [c] Database identifier code on the Cambridge Structural Database (CSD).

$TCVA^-$ = 1,2,2-tricyanoethenolate, and $TCNQ^{\bullet -}$ = 7,7′,8,8′-tetracyano-*p*-quinodimethanide radical. Similar to **1**, variable-temperature static magnetic susceptibility measurements confirmed strong antiferromagnetic coupling between Cu^{II} centres in complexes **2′–8**. Based on the J_{DFT} values obtained for **1′** and **2′–8**, the global hybrid GGA PBE0 density functional consistently yielded results in good agreement with experimental values (Fig. 6 and Table 3). Although complexes **7** and **8** exhibit additional magnetic exchange pathways *via* bridging ligands and weak non-covalent interactions such as π–π stacking, these interactions are beyond the scope of this study and are therefore not computed and discussed in detail (see SI).[115]

Magnetostructural correlation

A series of complexes **1′–8** was examined for magnetostructural correlations between the *J* values and various structural parameters. In the context of the superexchange mechanism, the magnetic properties of doubly pyrazolato-bridged Cu^{II} complexes are known to be influenced by multiple geometric factors.[70] A summary of key bond distances and angles is provided in Table S13. However, no clear correlation was observed between most geometric parameters and the experimentally/theoretically determined *J* values. Nevertheless, the *syn*-configuration complexes **1′**, **2′**, **3**, **5**, **7** and **8** exhibit larger negative *J* values than the *anti*-configuration complexes **4** and **6**, indicating stronger antiferromagnetic interaction due to more effective magnetic orbital overlap. Therefore, the nature of the apical ligand and the out-of-plane displacement of the Cu^{II} centre from the basal N_4 plane appear to influence the magnitude of *J*. Among all structural features examined, the intramolecular Cu–Cu distance *via* the doubly $bpypz^-$-bridging ligands exhibited the strongest correlation with *J*: shorter Cu–Cu distances consistently resulted in stronger antiferromagnetic coupling, reflecting enhanced orbital interaction across the bridging ligands. These results demonstrate that even subtle distortions—induced by apical ligand effects or geometric asymmetry—can have a substantial impact on the magnetic behaviour of doubly pyrazolato-bridged Cu^{II} complexes.

Conclusions

The dinuclear Cu^{II} complex, *syn*-$[Cu_2(\mu\text{-bpypz})_2Cl_{1.5}(H_2O)_{0.5}]$-$Cl_{0.5}\cdot 3H_2O$ (**1**) was synthesised by the reaction of $CuCl_2\cdot 2H_2O$ with Hbpypz in the mixed solvent of H_2O/MeOH under the solvothermal condition. The solid-state molecular structure of **1** was determined using SCXRD. The two Cu^{II} centres exhibited square pyramidal coordination geometries. One of the two Cu^{II} centres was bound equatorially by two independent $bpypz^-$ ligands, with chloride occupying the apical coordination site, whereas the other Cu^{II} centre featured a disordered chloride or water in the apical position. The apical chloride and/or water at the two Cu^{II} centres were *syn*-configurated to each other across the $Cu_2(\mu\text{-bpypz})_2$ basal plane. The DC molar magnetic susceptibility data for **1** revealed a strong antiferromagnetic coupling of $J = -191.52$ cm^{-1} *via* double $bpypz^-$-bridges, which is the same strength as that of the previously reported $Cu_2(\mu\text{-bpypz})_2$ family.

BS UKS-DFT calculations confirmed that the strong antiferromagnetic coupling was due to magnetic superexchange mediated by the $d_{x^2-y^2}$ orbitals of the Cu^{II} centres through the pyrazolate units within the double $bpypz^-$ bridges. A systematic evaluation of five density functionals (BP86, B3LYP, PBE0, TPSSh, and ωB97M-D3BJ) demonstrated that the PBE0 functional combined with the def2-TZVP basis set and ZORA relativistic approximation provided the most accurate predictions, highlighting its reliability in modelling the magnetic properties of doubly pyrazolate-bridged dinuclear Cu^{II} complexes.

Author contributions

R. I. formulated the project. R. I. and S. K. supervised the synthetic manipulation and directed the research. M. K. synthesised and characterised the compound. M. K. and R. I. collected and analysed the SCXRD data, with contributions from A. M. and S. K. R. I. collected the CW X-band ESR data. Y.-Y. W. and Z.-Y. L. collected the DC magnetic susceptibility data. R. I. interpreted the magnetic data and performed theoretical calculations. R. I. wrote the manuscript, with contributions from all authors.

Conflicts of interest

There are no conflict of interest.

Data availability

The data supporting this article have been included as part of the SI. Supplementary information: Experimental details, SCXRD measurement, computational details, PXRD, TGA, magnetic, CW X-band ESR spectral data. See DOI: **https://doi.org/10.1039/d5nj02006a**

CCDC 2445031 (**1**) contains the supplementary crystallographic data for this paper.[116]

Acknowledgements

This work was financially supported by JSPS KAKENHI Grant Number 20K05546 (S. K. and R. I.) and the Central Research Institute of Fukuoka University Grant Number GR2303 (R. I.). R. I. expresses their appreciation to the Research Project Grant, administered by FOERSTER JAPAN LIMITED, the Japan Research Institute of Industrial Science (Fukuyama), and the Iketani Science and Technology Foundation for their partial support of this research. We thank the referees for their insightful comments regarding the review process.

References

1 A. Bencini and D. Gatteschi, *Electron Paramagnetic Resonance of Exchange Coupled Systems*, Springer, Berlin, Heidelberg, 1990.
2 O. Kahn, *Molecular Magnetism*, VCH Publishers Inc., New York, 1993.
3 *Molecular Magnetism: From Molecular Assemblies to the Devices*, ed. E. Coronado, P. Delhaès, D. Gatteschi and J. S. Miller, Springer, Netherlands, Dordrecht, 1996.
4 *Molecular nanomagnets*, ed. D. Gatteschi, S. Roberta and J. Villain, Oxford University Press, New York, 2006.
5 W. Heisenberg, *Zeitschrift für Phys.*, 1928, **49**, 619–636.
6 J. H. van Vleck, *The Theory of Electric and Magnetic Susceptibilities*, Oxford University Press, London, 1932.
7 J. Klingele, S. Dechert and F. Meyer, *Coord. Chem. Rev.*, 2009, **253**, 2698–2741.
8 M. A. Halcrow, *Dalton Trans.*, 2009, 2059–2073.
9 M. Viciano-Chumillas, S. Tanase, L. J. de Jongh and J. Reedijk, *Eur. J. Inorg. Chem.*, 2010, 3403–3418.
10 J. García-Antón, R. Bofill, L. Escriche, A. Llobet and X. Sala, *Eur. J. Inorg. Chem.*, 2012, 4775–4789.
11 K. Ni-iya, A. Fuyuhiro, T. Yagi, S. Nasu, K. Kuzushita, S. Morimoto and S. Kaizaki, *Bull. Chem. Soc. Jpn.*, 2001, **74**, 1891–1897.
12 R. Kawahata, T. Tsukuda, T. Yagi, M. A. Subhan, H. Nakata, A. Fuyuhiro and S. Kaizaki, *Chem. Lett.*, 2003, **32**, 1084–1085.
13 C. Sens, I. Romero, M. Rodríguez, A. Llobet, T. Parella and J. Benet-Buchholz, *J. Am. Chem. Soc.*, 2004, **126**, 7798–7799.
14 R. Kawahata, T. Tsukuda, T. Yagi, A. Fuyuhiro and S. Kaizaki, *J. Alloys Compd.*, 2006, **408–412**, 976–980.
15 M.-L. Ho, Y.-M. Cheng, L.-C. Wu, P.-T. Chou, G.-H. Lee, F.-C. Hsu and Y. Chi, *Polyhedron*, 2007, **26**, 4886–4892.
16 A. Morioka-Yonezawa, N. Sakagami-Yoshida, A. Fuyuhiro and S. Kaizaki, *Inorganica Chim. Acta*, 2008, **361**, 3623–3630.
17 G. Gupta, G. P. A. Yap, B. Therrien and K. Mohan Rao, *Polyhedron*, 2009, **28**, 844–850.
18 F. Bozoglian, S. Romain, M. Z. Ertem, T. K. Todorova, C. Sens, J. Mola, M. Rodríguez, I. Romero, J. Benet-Buchholz, X. Fontrodona, C. J. Cramer, L. Gagliardi and A. Llobet, *J. Am. Chem. Soc.*, 2009, **131**, 15176–15187.
19 J. Mola, C. Dinoi, X. Sala, M. Rodríguez, I. Romero, T. Parella, X. Fontrodona and A. Llobet, *Dalton Trans.*, 2011, **40**, 3640–3646.
20 N. Planas, G. Christian, S. Roeser, E. Mas-Marzá, M.-R. Kollipara, J. Benet-Buchholz, F. Maseras and A. Llobet, *Inorg. Chem.*, 2012, **51**, 1889–1901.
21 M. L. Rigsby, S. Mandal, W. Nam, L. C. Spencer, A. Llobet and S. S. Stahl, *Chem. Sci.*, 2012, **3**, 3058–3062.
22 S. Fukuzumi, S. Mandal, K. Mase, K. Ohkubo, H. Park, J. Benet-Buchholz, W. Nam and A. Llobet, *J. Am. Chem. Soc.*, 2012, **134**, 9906–9909.
23 C. Krüger, H. Sato, T. Matsumoto, T. Shiga, G. N. Newton, F. Renz and H. Oshio, *Dalton Trans.*, 2012, **41**, 11270–11272.
24 S. Mandal, S. Shikano, Y. Yamada, Y.-M. Lee, W. Nam, A. Llobet and S. Fukuzumi, *J. Am. Chem. Soc.*, 2013, **135**, 15294–15297.
25 T. Ono, N. Planas, P. Miró, M. Z. Ertem, E. C. Escudero-Adán, J. Benet-Buchholz, L. Gagliardi, C. J. Cramer and A. Llobet, *ChemCatChem*, 2013, **5**, 3897–3903.
26 J. Graeupner, U. Hintermair, D. L. Huang, J. M. Thomsen, M. Takase, J. Campos, S. M. Hashmi, M. Elimelech, G. W. Brudvig and R. H. Crabtree, *Organometallics*, 2013, **32**, 5384–5390.
27 J. Aguiló, L. Francàs, H. J. Liu, R. Bofill, J. García-Antón, J. Benet-Buchholz, A. Llobet, L. Escriche and X. Sala, *Catal. Sci. Technol.*, 2014, **4**, 190–199.
28 L. Mognon, J. Benet-Buchholz, S. M. W. Rahaman, C. Bo and A. Llobet, *Inorg. Chem.*, 2014, **53**, 12407–12415.
29 S. Roeser, F. Bozoglian, C. J. Richmond, A. B. League, M. Z. Ertem, L. Francàs, P. Miró, J. Benet-Buchholz, C. J. Cramer and A. Llobet, *Catal. Sci. Technol.*, 2016, **6**, 5088–5101.
30 L. Mognon, S. Mandal, C. E. Castillo, J. Fortage, F. Molton, G. Aromí, J. Benet-Buchhlolz, M.-N. Collomb and A. Llobet, *Chem. Sci.*, 2016, **7**, 3304–3312.
31 T. Koizumi, Y. Ohkura and E. Tsuda, *Inorg. Chem. Commun.*, 2016, **67**, 25–28.
32 L. Francàs, C. Richmond, P. Garrido-Barros, N. Planas, S. Roeser, J. Benet-Buchholz, L. Escriche, X. Sala and A. Llobet, *Chem. – A Eur. J.*, 2016, **22**, 5261–5268.
33 S. Hennessey, P. Farràs, J. Benet-Buchholz and A. Llobet, *Catal. Sci. Technol.*, 2019, **9**, 6760–6768.
34 D. Hong, Y. Ohgomori, Y. Shimoyama, H. Kotani, T. Ishizuka, Y. Kon and T. Kojima, *Inorg. Chem.*, 2019, **58**, 11284–11288.
35 D. Hong, Y. Shimoyama, Y. Ohgomori, R. Kanega, H. Kotani, T. Ishizuka, Y. Kon, Y. Himeda and T. Kojima, *Inorg. Chem.*, 2020, **59**, 11976–11985.
36 J. Casabó, J. Pons, K. S. Siddiqi, F. Teixidor, E. Molins and C. Miravitlles, *J. Chem. Soc., Dalton Trans.*, 1989, 1401–1403.

37 J. Pons, X. López, J. Casabó, F. Teixidor, A. Caubet, J. Rius and C. Miravitlles, *Inorg. Chim. Acta*, 1992, **195**, 61–66.
38 M. Munakata, L. P. Wu, M. Yamamoto, T. Kuroda-Sowa, M. Maekawa, S. Kawata and S. Kitagawa, *J. Chem. Soc. Dalton Trans.*, 1995, 4099–4106.
39 N. Suemura, M. Ohama and S. Kaizaki, *Chem. Commun.*, 2001, 1538–1539.
40 K. Nakano, S. Kawata, K. Yoneda, A. Fuyuhiro, T. Yagi, S. Nasu, S. Morimoto and S. Kaizaki, *Chem. Commun.*, 2004, 2892–2893.
41 K. Nakano, N. Suemura, S. Kawata, A. Fuyuhiro, T. Yagi, S. Nasu, S. Morimoto and S. Kaizaki, *Dalton Trans.*, 2004, 982–988.
42 K. Nakano, N. Suemura, K. Yoneda, S. Kawata and S. Kaizaki, *Dalton Trans.*, 2005, 740–743.
43 C. J. Schneider, J. D. Cashion, B. Moubaraki, S. M. Neville, S. R. Batten, D. R. Turner and K. S. Murray, *Polyhedron*, 2007, **26**, 1764–1772.
44 M. Du, S.-T. Chen, Y.-M. Guo, X.-H. Bu and J. Ribas, *J. Mol. Struct.*, 2005, **737**, 17–21.
45 K. Yoneda, K. Adachi, S. Hayami, Y. Maeda, M. Katada, A. Fuyuhiro, S. Kawata and S. Kaizaki, *Chem. Commun.*, 2006, 45–47.
46 R. Ishikawa, A. Fuyuhiro, S. Hayami, K. Inoue and S. Kawata, *J. Mol. Struct.*, 2008, **892**, 220–224.
47 J.-F. Létard, C. Carbonera, J. A. Real, S. Kawata and S. Kaizaki, *Chem. – Eur. J.*, 2009, **15**, 4146–4155.
48 A. Mishima, A. Fuyuhiro, H. Kumagai and S. Kawata, *Acta Crystallogr., Sect. E:Struct. Rep. Online*, 2011, **67**, m1523–m1524.
49 R. Ishikawa, K. Nishio, A. Fuyuhiro, K. Yoneda, H. Sakamoto, S. Kitagawa and S. Kawata, *Inorg. Chim. Acta*, 2012, **386**, 122–128.
50 T. Washizaki, R. Ishikawa, K. Yoneda, S. Kitagawa, S. Kaizaki, A. Fuyuhiro and S. Kawata, *RSC Adv.*, 2012, **2**, 12169–12172.
51 A. Mishima, N. Katsuta, M. Furusyou, A. Fuyuhiro and S. Kawata, *Acta Crystallogr., Sect. E:Struct. Rep. Online*, 2013, **69**, m455–m456.
52 N. Katsuta, A. Mishima, A. Fuyuhiro, S. Hayami and S. Kawata, *Acta Crystallogr., Sect. E:Struct. Rep. Online*, 2013, **69**, m574.
53 M. Sy, F. Varret, K. Boukheddaden, G. Bouchez, J. Marrot, S. Kawata and S. Kaizaki, *Angew. Chem., Int. Ed.*, 2014, **53**, 7539–7542.
54 R. Ishikawa, S. Ueno, Y. Hamatake, Y. Horii, Y. Miyazaki, M. Nakano, T. Noda, M. Uematsu and S. Kawata, *CrystEngComm*, 2019, **21**, 1886–1894.
55 R. Ishikawa, S. Ueno, H. Iguchi, B. K. Breedlove, M. Yamashita and S. Kawata, *CrystEngComm*, 2020, **22**, 159–163.
56 J. Soldevila-Sanmartín, T. Calvet, M. Font-Bardia, J. G. Planas and J. Pons, *Polyhedron*, 2022, **211**, 115543.
57 K. Yoneda, K. Adachi, K. Nishio, M. Yamasaki, A. Fuyuhiro, M. Katada, S. Kaizaki and S. Kawata, *Angew. Chem., Int. Ed.*, 2006, **45**, 5459–5461.
58 J.-Z. Hou, M. Li, Z. Li, S.-Z. Zhan, X.-C. Huang and D. Li, *Angew. Chem., Int. Ed.*, 2008, **47**, 1711–1714.
59 R. Ishikawa, M. Nakano, A. Fuyuhiro, T. Takeuchi, S. Kimura, T. Kashiwagi, M. Hagiwara, K. Kindo, S. Kaizaki and S. Kawata, *Chem. – Eur. J.*, 2010, **16**, 11139–11144.
60 S. Romain, J. Rich, C. Sens, T. Stoll, J. Benet-Buchholz, A. Llobet, M. Rodriguez, I. Romero, R. Clérac, C. Mathonière, C. Duboc, A. Deronzier and M.-N. Collomb, *Inorg. Chem.*, 2011, **50**, 8427–8436.
61 M. Okamura, M. Kondo, R. Kuga, Y. Kurashige, T. Yanai, S. Hayami, V. K. K. Praneeth, M. Yoshida, K. Yoneda, S. Kawata and S. Masaoka, *Nature*, 2016, **530**, 465.
62 E. Gouré, B. Gerey, M. Clémancey, J. Pécaut, F. Molton, J.-M. Latour, G. Blondin and M.-N. Collomb, *Inorg. Chem.*, 2016, **55**, 9178–9186.
63 E. Gouré, B. Gerey, F. Molton, J. Pécaut, R. Clérac, F. Thomas, J. Fortage and M.-N. Collomb, *Inorg. Chem.*, 2020, **59**, 9196–9205.
64 T. Akai, M. Kondo, S. K. Lee, H. Izu, T. Enomoto, M. Okamura, Y. Saga and S. Masaoka, *Dalton Trans.*, 2020, **49**, 1384–1387.
65 P. Pelosin, M. Gil-Sepulcre, P. Garrido-Barros, D. Moonshiram, J. Benet-Buchholz, C. Gimbert-Suriñach and A. Llobet, *iScience*, 2020, **23**, 101378.
66 E. Gouré, B. Gerey, J. Pécaut, F. Thomas, J. Fortage and M.-N. Collomb, *ChemElectroChem*, 2021, **8**, 2912–2920.
67 M. Tomoda, M. Kondo, H. Izu and S. Masaoka, *Chem. –A Eur. J.*, 2023, **29**, e202203253.
68 T. Akai, Y. Iwamura, M. Kondo, Y. Saga and S. Masaoka, *Chem. Lett.*, 2023, **52**, 211–214.
69 H. Izu, M. Kondo, M. Okamura, M. Tomoda, S. K. Lee, T. Akai, V. K. K. Praneeth, M. Kanaike, S. Kawata and S. Masaoka, *Angew. Chem., Int. Ed.*, 2024, **63**, e202408514.
70 I. Castro, W. P. Barros, M. L. Calatayud, F. Lloret, N. Marino, G. De Munno, H. O. Stumpf, R. Ruiz-García and M. Julve, *Coord. Chem. Rev.*, 2016, **315**, 135–152.
71 S. Luo, C. Xu, R. Zhang and X. Sun, *Chem. Phys. Lett.*, 2021, **784**, 139102.
72 A. P. Ginsberg, *J. Am. Chem. Soc.*, 1980, **102**, 111–117.
73 L. Noodleman, *J. Chem. Phys.*, 1981, **74**, 5737–5743.
74 L. Noodleman and E. R. Davidson, *Chem. Phys.*, 1986, **109**, 131–143.
75 *Applied Quantum Chemistry*, ed. V. H. Smith, H. F. Schaefer and K. Morokuma, Springer, Netherlands, Dordrecht, 1986.
76 K. Yamaguchi, T. Tsunekawa, Y. Toyoda and T. Fueno, *Chem. Phys. Lett.*, 1988, **143**, 371–376.
77 A. Bencini, F. Totti, C. A. Daul, K. Doclo, P. Fantucci and V. Barone, *Inorg. Chem.*, 1997, **36**, 5022–5030.
78 E. Ruiz, J. Cano, S. Alvarez and P. Alemany, *J. Comput. Chem.*, 1999, **20**, 1391–1400.
79 A. W. Addison, T. N. Rao, J. Reedijk, J. van Rijn and G. C. Verschoor, *J. Chem. Soc., Dalton Trans.*, 1984, 1349–1356.
80 F. A. Chavez, M. M. Olmstead and P. K. Mascharak, *Inorg. Chem.*, 1996, **35**, 1410–1412.
81 S. Roy, P. Mitra and A. K. Patra, *Inorg. Chim. Acta*, 2011, **370**, 247–253.
82 B. Bleaney and K. D. Bowers, *Proc. R. Soc. London. Ser. A. Math. Phys. Sci.*, 1952, **214**, 451–465.
83 N. F. Chilton, R. P. Anderson, L. D. Turner, A. Soncini and K. S. Murray, *J. Comput. Chem.*, 2013, **34**, 1164–1175.

84 B. O. Roos, P. R. Taylor and P. E. M. Sigbahn, *Chem. Phys.*, 1980, **48**, 157–173.
85 K. Andersson, P. A. Malmqvist, B. O. Roos, A. J. Sadlej and K. Wolinski, *J. Phys. Chem.*, 1990, **94**, 5483–5488.
86 K. Andersson, P. Malmqvist and B. O. Roos, *J. Chem. Phys.*, 1992, **96**, 1218–1226.
87 C. Angeli, R. Cimiraglia, S. Evangelisti, T. Leininger and J.-P. Malrieu, *J. Chem. Phys.*, 2001, **114**, 10252–10264.
88 C. Angeli, R. Cimiraglia and J.-P. Malrieu, *J. Chem. Phys.*, 2002, **117**, 9138–9153.
89 G. K.-L. Chan and S. Sharma, *Annu. Rev. Phys. Chem.*, 2011, **62**, 465–481.
90 K. H. Marti and M. Reiher, *Phys. Chem. Chem. Phys.*, 2011, **13**, 6750–6759.
91 R. Olivares-Amaya, W. Hu, N. Nakatani, S. Sharma, J. Yang and G. K.-L. Chan, *J. Chem. Phys.*, 2015, **142**, 34102.
92 T. Yanai, Y. Kurashige, W. Mizukami, J. Chalupský, T. N. Lan and M. Saitow, *Int. J. Quantum Chem.*, 2015, **115**, 283–299.
93 M. Roemelt and D. A. Pantazis, *Adv. Theory Simulations*, 2019, **2**, 1800201.
94 J. Miralles, J.-P. Daudey and R. Caballol, *Chem. Phys. Lett.*, 1992, **198**, 555–562.
95 J. Miralles, O. Castell, R. Caballol and J.-P. Malrieu, *Chem. Phys.*, 1993, **172**, 33–43.
96 G. Singh, S. Gamboa, M. Orio, D. A. Pantazis and M. Roemelt, *Theor. Chem. Acc.*, 2021, **140**, 139.
97 F. A. Evangelista, *J. Chem. Phys.*, 2018, **149**, 30901.
98 A. Khedkar and M. Roemelt, *Phys. Chem. Chem. Phys.*, 2021, **23**, 17097–17112.
99 F. Neese, *Wiley Interdiscip. Rev.: omput. Mol. Sci.*, 2012, **2**, 73–78.
100 F. Neese, *Wiley Interdiscip. Rev.: omput. Mol. Sci.*, 2018, **8**, e1327.
101 J. G. Brandenburg, C. Bannwarth, A. Hansen and S. Grimme, *J. Chem. Phys.*, 2018, **148**, 64104.
102 D. A. Pantazis, X.-Y. Chen, C. R. Landis and F. Neese, *J. Chem. Theory Comput.*, 2008, **4**, 908–919.
103 F. Weigend, *Phys. Chem. Chem. Phys.*, 2006, **8**, 1057–1065.
104 C. van Wüllen, *J. Chem. Phys.*, 1998, **109**, 392–399.
105 A. D. Becke, *Phys. Rev. A: At., Mol., Opt. Phys.*, 1988, **38**, 3098–3100.
106 J. P. Perdew, *Phys. Rev. B: Condens. Matter Mater. Phys.*, 1986, **33**, 8822–8824.
107 V. N. Staroverov, G. E. Scuseria, J. Tao and J. P. Perdew, *J. Chem. Phys.*, 2003, **119**, 12129–12137.
108 A. D. Becke, *J. Chem. Phys.*, 1993, **98**, 5648–5652.
109 P. J. Stephens, F. J. Devlin, C. F. Chabalowski and M. J. Frisch, *J. Phys. Chem.*, 1994, **98**, 11623–11627.
110 C. Adamo and V. Barone, *J. Chem. Phys.*, 1999, **110**, 6158–6170.
111 M. Ernzerhof and G. E. Scuseria, *J. Chem. Phys.*, 1999, **110**, 5029–5036.
112 A. Najibi and L. Goerigk, *J. Chem. Theory Comput.*, 2018, **14**, 5725–5738.
113 N. A. G. Bandeira and B. Le Guennic, *J. Phys. Chem. A*, 2012, **116**, 3465–3473.
114 N. Manukovsky, G. Kamieniarz and L. Kronik, *J. Chem. Phys.*, 2023, **159**, 154103.
115 M. Shoji, K. Koizumi, Y. Kitagawa, T. Kawakami, S. Yamanaka, M. Okumura and K. Yamaguchi, *Chem. Phys. Lett.*, 2006, **432**, 343–347.
116 M. Kawano, Y.-Y. Wu, Z.-Y. Li, A. Mishima, S. Kawata and R. Ishikawa, CCDC 2445031: Experimental Crystal Structure Determination, 2025, DOI: **10.5517/ccdc.csd.cc2n27zz**.